(Received 30 August 2025, Accepted 31 October 2025, Scheduled 11 November 2025)

Enhanced Vibration Compensation for CCR-BIM: RA-SOGI Observer with Variable Step-Size Adaptive LMS and Residual-Feedforward Adaptive PID

Chengling Lu[1,*], Ziqing Liu[1,2], Wenxin Fang[3], Qifeng Ding[4], and Yanxue Zhang[1]

[1] *School of Electrical and Photoelectric Engineering, West Anhui University, Lu'An 237012, China*
[2] *Motor Engineering Research Center, Lu'An Jianghuai Motor Co., Lu'An 237012, China*
[3] *Institute of Agricultural Facilities and Equipment, Jiangsu Academy of Agricultural Sciences, Nanjing 210008, China*
[4] *School of Electrical Information Engineering, Jiangsu University, Zhenjiang 212013, China*

ABSTRACT: To mitigate unbalanced vibration caused by rotor eccentricity in composite cage rotor bearingless induction motors (CCR-BIM), this paper proposes an enhanced hybrid control strategy integrating a rotor-speed adaptive second-order generalized integrator (RA-SOGI) harmonic observer with dual-channel compensation. A variable step-size adaptive LMS (VSS-ALMS) algorithm is introduced to optimize RA-SOGI, enabling real-time extraction of fundamental vibration components with reduced computational burden and improved convergence. In the feedback channel, an adaptive PID controller with variable learning rates and residual feedforward correction is designed, achieving a superior balance between transient response and steady-state precision. Lyapunov-based analysis establishes the global asymptotic stability of the proposed scheme under practical step-size constraints. Experimental validations demonstrate that the proposed method significantly outperforms conventional PID and feedforward control, achieving faster convergence, higher vibration attenuation, and enhanced trajectory stability in high-speed CCR-BIM operation.

1. INTRODUCTION

Bearingless induction motor (BIM) is a novel type of motor that utilizes controllable suspension force to suspend the rotor within the stator without physical contact. BIM offers advantages such as operation without mechanical friction, no wear, no need for lubrication, high speed, high precision, and long lifespan [1–4]. Currently, BIM demonstrates broad application prospects in fields such as energy storage systems, chemical processing, and high-speed rotating machinery [5, 6].

As one extended type of BIM, composite cage rotor bearingless induction motor (CCR-BIM) combines the features of BIM and composite rotor induction motors. It exhibits excellent starting performance and suspension performance [7–9]. In CCR-BIM, real-time monitoring of the composite cage rotor's displacement is essential. However, due to factors such as machining errors and magnetic asymmetry, the rotor's center of mass inevitably deviates from its geometric center, resulting in unbalanced vibrations during operation [10–12]. Consequently, the displacement sensor signals transmitted to the controller inherently contain these unbalanced vibration components. To mitigate the adverse effects of such vibrations on system stability, vibration compensation control technology must be employed to extract unbalanced vibration signals and generate counteracting compensation forces [13, 14].

With the advancement of control technologies, traditional induction motor regulation strategies have been further optimized, and various vibration compensation control methods have been proposed to mitigate rotor imbalance vibrations. For example, sliding mode control (SMC) combined with space vector PWM (SVPWM) modulation has been employed to enhance the dynamic speed response of induction motors under varying load conditions [15]. Meanwhile, various vibration compensation control methods have been proposed to mitigate rotor imbalance vibrations. Ref. [16] proposed a vibration compensation control method based on a fuzzy coefficient adaptive linear neuron (FCALN) algorithm, which decomposes displacement signals to extract vibration-related harmonic components. This FCALN-based approach was comparatively analyzed against conventional proportional integral differential (PID) vibration compensation methods. Ref. [17] proposed an unbalanced vibration compensation control approach based on an extended Kalman filter (EKF). Ref. [18] proposed a hybrid vibration compensation strategy combining feedforward compensation with current compensation. Ref. [19] proposed an unbalanced vibration suppression control strategy based on an improved total least squares (TLS) algorithm, where modifications to the cost function of the TLS adaptive filtering algorithm enhanced its anti-disturbance performance. Ref. [20] proposed an adaptive least mean square (LMS)-based unbalanced displacement extraction method that enables rapid displacement detection and improves the magnetic levitation control performance of bearingless induction motors. Ref. [21] proposed a model-compensated linear active disturbance rejection control method that effectively reduces rotor displacement and torque ripple. Ref. [22] proposed a feed-forward compensation control strategy based on a parameter-free variable

* Corresponding author: Chengling Lu (luchengling@wxc.edu.cn).

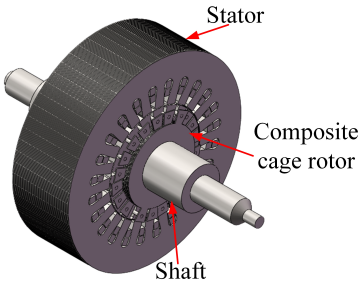

FIGURE 1. Topology of CCR-BIM.

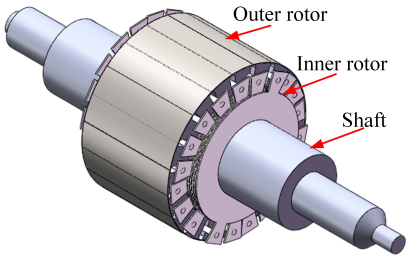

FIGURE 2. Structure of the composite cage rotor.

step-size LMS (VSS-LMS) adaptive filter. By replacing variable parameters in the step-size function with error signal accumulation, this strategy resolves the inherent trade-off between convergence speed and steady-state error in conventional LMS algorithms, while simultaneously addressing the excessive iteration steps issue in VSS-LMS implementations. Although the above-mentioned vibration compensation strategy can effectively suppress rotor vibration, the extraction of harmonics is rather complicated, which often leads to a huge amount of computation and thus poor real-time performance. Moreover, the traditional PID control has deficiencies in signal regulation capability.

To overcome these challenges, this paper proposes an enhanced hybrid vibration compensation framework combining a rotor-speed adaptive second-order generalized integrator (RA-SOGI) harmonic observer with advanced dual-channel compensation. The main contributions are summarized as follows:

(1) A VSS-ALMS-enhanced RA-SOGI harmonic observer that achieves real-time extraction of fundamental vibration components while reducing computational complexity and improving convergence robustness.

(2) An adaptive PID controller with variable learning rates and residual feedforward correction, which dynamically adjusts amplitude and phase while leveraging residual information to anticipate unmodeled disturbances, thereby balancing transient response and steady-state accuracy.

(3) A Lyapunov-based stability analysis that theoretically proves global asymptotic stability of the proposed compensation scheme under practical step-size constraints.

The remainder of this paper is organized as follows. Section 2 describes the vibration mechanism and mathematical modeling of the CCR-BIM. Section 3 details the design of the RA-SOGI harmonic observer and the dual-channel adaptive compensation strategy. Section 4 reports the experimental results and performance evaluation, and Section 5 summarizes the conclusions and outlines future work.

2. MODELING OF THE CCR-BIM VIBRATION MECHANISM

2.1. Structure and Suspension Mechanism

CCR-BIM utilizes the structural similarity between magnetic bearings and induction motor stators by incorporating a set of three-phase suspension winding with torque winding. The CCR-BIM primarily consists of a stator, a composite cage rotor, and auxiliary components such as a rotating shaft. The overall topology of the CCR-BIM is illustrated in Fig. 1.

The composite cage rotor comprises an inner rotor and an outer rotor. The inner rotor is composed of a rotor core, a cage rotor, and end rings. The cage structure of the inner rotor is specially designed to shield the suspension force winding while only inducing torque winding [23]. The outer rotor is a solid layer with high magnetic permeability. Owing to the skin effect, the induced current density is concentrated near the surface of the silicon steel layer, which facilitates the generation of higher starting torque. This helps the motor overcome significant resistance during startup, achieving rapid acceleration and enhancing the starting performance of the CCR-BIM. The structure is depicted in Fig. 2.

The stator of the CCR-BIM consists of a stator core and windings, as shown in Fig. 3(a). The stator slots accommodate two sets of windings: torque winding and suspension force winding. Torque winding provides driving torque to the composite cage rotor, while suspension force winding generates radial levitation force to maintain stable self-suspension of the rotor. In the CCR-BIM stator, both windings adopt a single-layer concentric distribution. The torque winding and suspen-

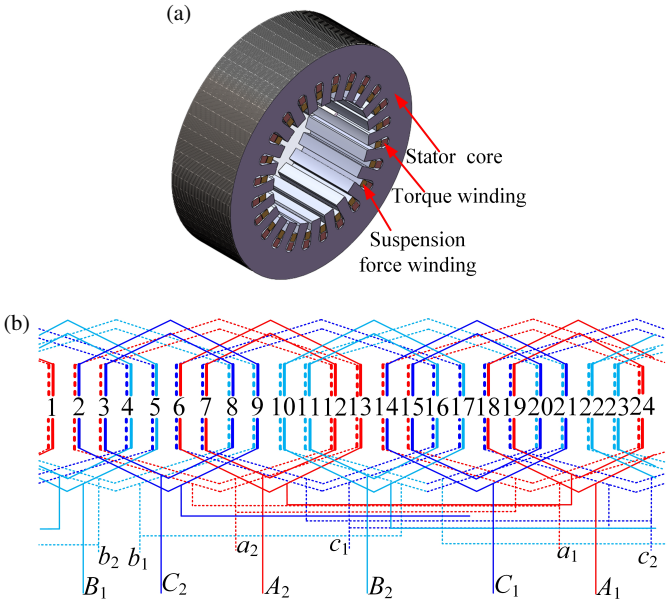

FIGURE 3. Stator structure and winding distribution. (a) Stator structure. (b) Winding distribution.

sion force winding are powered by two separate inverter power supplies, respectively. The stator has 24 slots. The dashed lines represent the torque winding distribution, with terminals labeled as a_1 and a_2, b_1 and b_2, c_1 and c_2. Based on the winding configuration, pole pairs of the torque winding (p_1) are determined to be 1. The solid lines represent the suspension force winding distribution, with terminals labeled as A_1 and A_2, B_1 and B_2, C_1 and C_2, and its pole pairs (p_2) are determined to be 2. The torque winding is placed at the bottom of the stator slots, while the suspension force winding is located at the top. The stator winding distribution is illustrated in Fig. 3(b).

Electromagnetic torque and radial suspension forces are generated through the interaction between the magnetic fields of these two sets of windings. When the two windings satisfy the conditions $p_1 = p_2 \pm 1$ and $\omega_1 = \omega_2$, the CCR-BIM can produce controllable suspension forces, where p_1, ω_1 and p_2, ω_2 denote the number of pole pairs and angular frequency of the torque winding and suspension winding, respectively. As shown in Fig. 4, currents I_1 and I_2 are applied to the torque winding and suspension winding, respectively, generating magnetic fluxes ψ_1 and ψ_2. The magnetic flux is enhanced in the positive y-axis direction while being weakened in the negative y-axis direction. Consequently, the resultant magnetic flux vector points along the positive y-axis, leading to a net suspension force also directed along the positive y-axis. By reversing the current direction in the windings, a controllable suspension force along the negative y-axis can be obtained, thereby achieving controlled suspension along the horizontal degree of freedom of the CCR-BIM rotor. A similar analysis is applied to the generation of controllable suspension forces along the x-axis [24–27].

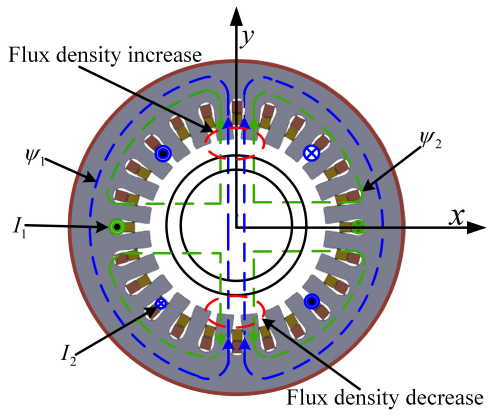

FIGURE 4. Suspension force generation in CCR-BIM.

2.2. Mathematical Model

The expressions for the suspension forces in the x-direction and y-direction are [16]:

$$\begin{bmatrix} F_{cx} \\ F_{cy} \end{bmatrix} = F_m \begin{bmatrix} i_{2d} & i_{2q} \\ i_{2q} & -i_{2d} \end{bmatrix} \begin{bmatrix} \psi_{1d} \\ \psi_{1q} \end{bmatrix}, \tag{1}$$

where i_{2d} and i_{2q} are the d-axis and q-axis components of the stator current in the suspension force winding, respectively; ψ_{1d} and ψ_{1q} represent the d-axis and q-axis rotor flux components of the torque winding, respectively; F_m is the amplitude of the suspension force.

The torque equation of the CCR-BIM is expressed as:

$$T_e = i_{1q}\psi_{1d} - i_{1d}\psi_{1q}, \tag{2}$$

where i_{1d} and i_{1q} are the d-axis and q-axis current components of the torque winding, respectively; ψ_{1d} and ψ_{1q} represent the d-axis and q-axis flux linkages of the torque winding, respectively.

2.3. Rotor Unbalance Vibration Mechanism

During the operation of the CCR-BIM, manufacturing tolerances cause a deviation between the rotor's center of mass and its geometric center (denoted as $\Delta r = |O - O'|$), leading to a mass imbalance phenomenon. The dynamic characteristics of the unbalanced force F_c can be quantitatively characterized by the centrifugal force equation [19]:

$$F_c = m\omega_m^2 \Delta r, \tag{3}$$

where m is the rotor mass, and ω_m is the mechanical angular velocity of the rotor. It can be observed that F_c increases quadratically with ω_m, implying that even a minor eccentricity Δr can lead to significant periodic excitation at high speeds.

The dynamic coordinate system established to characterize the physical mechanism of rotor eccentricity is illustrated in Fig. 5. In this figure, point O represents the geometric center of the CCR-BIM, while point O' denotes the rotor's center of mass. Due to manufacturing tolerances, these two points do not coincide. The stationary reference frame is defined by the horizontal axis x and vertical axis y, whereas the rotating reference frame is represented by the d-axis and q-axis. Within the fixed (x, y) coordinate system, the deviation between the geometric center O and the center of mass O' forms a rotating vector Δr, whose phase angle η varies at the electrical angular velocity ω_e of the rotating d-q frame.

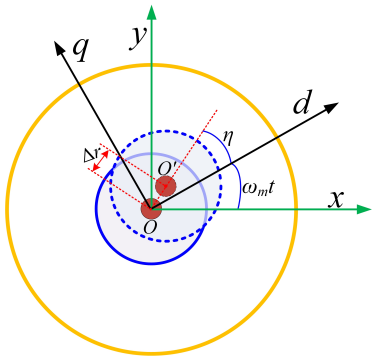

FIGURE 5. Rotor eccentricity coordinate system.

The unbalanced vibrational force F_c can be decomposed into orthogonal components along the fixed coordinate axes, denoted as F_{cx} and F_{cy}, and expressed as:

$$\begin{cases} F_{cx} = F_c \cos(\omega_e t + \eta) \\ F_{cy} = F_c \sin(\omega_e t + \eta) \end{cases}, \tag{4}$$

where η is the angle between the line connecting the geometric center to the center of mass and the d-axis, and ω_e is the electrical angular velocity, given by $\omega_e = p_1\omega_m$. Since $p_1 = 1$,

$\omega_e = \omega_m$, and thus the mechanical angular velocity will substitute for the electrical angular velocity in subsequent discussions.

Let the unbalanced vibration displacement components along the x-axis and y-axis be denoted as x_c and y_c, respectively. The vibration displacements along the x-axis and y-axis induced by the unbalanced force F_c can be expressed as:

$$\begin{cases} x_c = A\cos(\omega_m t + \eta - \gamma) \\ y_c = A\sin(\omega_m t + \eta - \gamma) \end{cases}, \tag{5}$$

where A is the vibration amplitude, and γ is the phase lag angle between the unbalanced vibration displacement and unbalanced force.

In summary, from Eqs. (3)–(5), unbalanced force F_c is proportional to rotor mass m, rotor eccentricity Δr, and the square of the mechanical angular velocity ω_m. Periodic unbalanced forces and corresponding displacement components exist along both the x-axis and y-axis, with a frequency of ω_m. Therefore, the unbalanced force F_c increases with rotational speed, and without compensation, the system will become unstable.

3. DESIGN OF RA-SOGI-BASED ADAPTIVE COMPENSATION STRATEGY

As analyzed in the previous section, the primary source of rotor unbalanced force is the periodic unbalanced force F_c that occurs at the same frequency as the electrical angular velocity ω_e. Consequently, the core objective of vibration compensation control is to achieve dynamic compensatory force generation through real-time extraction of fundamental frequency components, thereby canceling out the disturbances caused by F_c. To address the limitations of conventional methods, this section presents a hybrid control strategy combining an improved rotor-speed adaptive second order generalized integrator (RA-SOGI)-based harmonic observer with a dual-channel adaptive PID controller. The RA-SOGI harmonic observer directly locks onto the fundamental frequency component corresponding to ω_e, while the dual-channel adaptive PID dynamically optimizes both the amplitude and phase of the compensatory force, achieving real-time suppression of rotor vibrations [28, 29].

3.1. Harmonic Observer Design and Principle

3.1.1. SOGI-Based Harmonic Observer Implementation

Accurate real-time harmonic extraction is a critical component of vibration compensation control. The conventional second order generalized integrator (SOGI) can isolate the fundamental frequency component synchronized with the mechanical angular velocity ω_m from noise-contaminated displacement signals through quadrature signal generation and frequency adaptation mechanisms. However, its fixed damping ratio and gain design lead to insufficient dynamic performance under sudden speed variations or load disturbances. To address this limitation, this study proposes an improved RA-SOGI harmonic observer, which introduces a nonlinear damping adjustment mechanism and a dynamic frequency tracking algorithm to enhance real-time performance and robustness in harmonic extraction.

The raw displacement signal $v(k)$ contains high-frequency noise and sensor interference, and therefore requires preprocessing with a second order butterworth low-pass filter (LPF). The cutoff frequency of the LPF is set to $1.2\omega_m$, thereby effectively suppressing high-frequency noise while preserving the integrity of the fundamental frequency component at ω_m.

The standard transfer function of a second order Butterworth low-pass filter is given as:

$$H(s) = \frac{\omega_c^2}{s^2 + \sqrt{2}\omega_c s + \omega_c^2}, \tag{6}$$

where ω_c is the cutoff angular frequency, and $\omega_c = 1.2\omega_m$.

Equation (6) can be rewritten as:

$$H_{\mathbf{LPF}}(s) = \frac{(1.2\omega_m)^2}{s^2 + \sqrt{2}\cdot 1.2\omega_m \cdot s + (1.2\omega_m)^2}. \tag{7}$$

The transfer function in Eq. (7) is discretized into a time-domain difference equation using a discretization method, where $s = \frac{2}{T}\cdot\frac{z-1}{z+1}$, and T denotes the sampling period. The final discretized difference equation is expressed as:

$$\begin{aligned} v_f(k) = {} & a_1 v_f(k-1) + a_2 v_f(k-2) \\ & + b_0 v(k) + b_1 v(k-1) + b_2 v(k-2). \end{aligned} \tag{8}$$

The filter coefficients a_1, a_2, b_0, b_1, b_2 are dynamically updated based on ω_m, calculated using the following expressions:

$$\begin{cases} K = \tan\left(\frac{1.2\omega_m T}{2}\right) \\ b_0 = b_2 = \frac{K^2}{1+\sqrt{2}K+K^2} \\ b_1 = 2b_0 \\ a_1 = \frac{2(K^2-1)}{1+\sqrt{2}K+K^2} \\ a_2 = \frac{1-\sqrt{2}K+K^2}{1+\sqrt{2}K+K^2} \end{cases}, \tag{9}$$

3.1.2. RA-SOGI Harmonic Observer with Nonlinear Gain Regulation

To further reduce computational complexity and facilitate digital implementation, this study introduces an equivalent realization of the RA-SOGI based on quadrature demodulation, which preserves its observation capability while alleviating the computational burden without compromising performance.

The filtered signal $v_f(k)$ serves as the input to the SOGI block. The conventional SOGI's transfer functions are given by:

$$\begin{cases} H_\alpha(s) = \frac{v_\alpha(s)}{v_f(s)} = \frac{\xi\omega_m s}{s^2+\xi\omega_m s+\omega_m^2} \\ H_\beta(s) = \frac{v_\beta(s)}{v_f(s)} = \frac{\xi\omega_m^2}{s^2+\xi\omega_m s+\omega_m^2} \end{cases}, \tag{10}$$

where ξ is the damping coefficient, s the Laplace operator, $v_f(s)$ the input displacement signal, $v_\alpha(s)$ the in-phase output corresponding to the fundamental displacement component, and $v_\beta(s)$ the quadrature output corresponding to the same component.

With a fixed damping ratio ξ and constant gain, this structure relies solely on ω_m. In order to enhance the robustness and adaptability of the harmonic observer under varying rotor speeds and disturbances, an improved rotor-speed adaptive second order generalized integrator (RA-SOGI) with nonlinear gain regulation is designed. We replace the fixed damping ratio ξ with an adaptive damping function $\xi(t)$, and the dynamic equations are formulated as:

$$\xi(t) = \xi_0 + \Delta\xi \cdot \mathbf{sat}\left(\frac{|v_f(t) - v_\alpha(t)|}{\epsilon}\right), \tag{11}$$

where ξ_0 represents the baseline damping, with a value of 0.8; $\Delta\xi$ represents the maximum damping variation, with a value of 0.4; ϵ represents the error threshold, with a value of 0.2 μm; **sat**$(\cdot)$ represents the saturation function used to limit $\xi(t) \in [\xi_0,\ \xi_0 + \Delta\xi]$. Parameters ξ_0, $\Delta\xi$, ϵ were empirically tuned to achieve a balance between convergence speed and steady-state accuracy in the harmonic extraction.

The corresponding state-space implementation becomes:

$$\begin{cases} \dot{v}_\alpha = -\xi(t)\omega_m v_\beta + \xi(t)\omega_m(v_f - v_\alpha) \\ \dot{v}_\beta = \xi(t)\omega_m(v_f - v_\alpha) \end{cases}, \tag{12}$$

To implement real-time digital filtering, the transfer function is discretized into a time-domain difference equation. The time-domain representation of the SOGI is given by:

$$\begin{cases} v_\alpha(k) = \frac{2-\xi T\omega_m}{2+\xi T\omega_m} v_\alpha(k-1) \\ \qquad + \frac{\xi T\omega_m}{2+\xi T\omega_m}[v_f(k) + v_f(k-1)] \\ v_\beta(k) = \frac{2-\xi T\omega_m}{2+\xi T\omega_m} v_\beta(k-1) \\ \qquad + \frac{\xi T\omega_m}{2+\xi T\omega_m}[v_f(k) + v_f(k-1)] \end{cases}, \tag{13}$$

This discretization method approximates the integral terms using trapezoidal summation, avoiding numerical oscillations commonly seen in traditional Euler methods, thereby enhancing algorithm stability.

3.1.3. Frequency Adaptive Adjustment Mechanism

When the rotor speed varies, the center frequency ω_m of the RA-SOGI must also be dynamically updated to maintain harmonic locking. The update formula is given by:

$$\begin{cases} \omega_m = \frac{2\pi n}{60} \\ f_m = \frac{n}{60} \end{cases}, \tag{14}$$

where n denotes the rotor speed.

The raw displacement signal $v(k)$, collected from the rotor displacement sensor, contains both the fundamental vibration component and noise. To simplify computation, quadrature modulation is employed to directly decompose the fundamental component, replacing the filtered output of the standard SOGI.

The prefiltered signal $v_f(k)$ is fed into the RA-SOGI to generate the in-phase signal $\nu_\alpha(k)$ and quadrature signal $\nu_\beta(k)$ of the fundamental component. Their discrete-time expressions are:

$$\begin{cases} v_\alpha(k) = v_f(k)\cos(\omega_m kT) \\ v_\beta(k) = v_f(k)\sin(\omega_m kT) \end{cases}. \tag{15}$$

It is worth noting that the proposed RA-SOGI observer replaces the conventional SOGI structure with a simplified quadrature demodulation method to extract the in-phase (v_α) and quadrature (v_β) components.

(2) Harmonic Reconstruction

The quadrature components are then combined to reconstruct the complete fundamental harmonic component $v_h(k)$, expressed as:

$$v_h(k) = \sqrt{v_\alpha^2(k) + v_\beta^2(k)} \cdot \cos(\omega_m kT + \phi), \tag{16}$$

where $\phi = \arctan(\frac{v_\beta(k)}{v_\alpha(k)})$ is the instantaneous phase angle.

By updating ω_m in real time using the frequency adaptation mechanism in Eq. (12), the harmonic component's amplitude $\sqrt{v_\alpha^2(k) + v_\beta^2(k)}$ and phase ϕ remain synchronized with the rotor speed, enabling dynamic tracking of the vibration excitation source.

The displacement error signal $e(k)$ is obtained by subtracting the fundamental harmonic component from the original displacement signal:

$$e(k) = v_{ref}(k) - v_h(k), \tag{17}$$

where v_{ref} is the desired displacement reference, typically set to zero.

The resulting error signal $e_{(k)}$ serves as the input to the adaptive PID controller, which dynamically corrects residual vibrations through the feedback channel.

The overall flowchart of the harmonic component extraction and displacement error generation process is illustrated in Fig. 6.

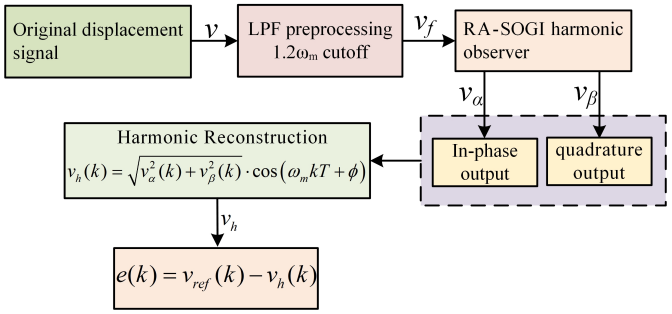

FIGURE 6. Flowchart of harmonic component extraction and displacement error signal generation.

3.2. Variable Step-Size Adaptive LMS-Based Compensation Design

The periodic exciting force caused by rotor unbalance vibration needs to be dynamically counteracted by a compensation force. However, due to variations in rotational speed, load changes, and noise interference, the amplitude and phase of the compensation force must be adjusted in real time. The adaptive compensation design presented in this section is achieved by dynamically adjusting the amplitude and phase of the compensation force using a VSS-ALMS algorithm, thereby canceling out the rotor vibration and ensuring the stability of the CCR-BIM suspension system [30, 31].

3.2.1. Variable Step-Size Adaptive LMS Algorithm

The conventional Least Mean Square (LMS) algorithm minimizes the mean square value of displacement error by adjusting a multidimensional weight vector. Its update rule is expressed as:

$$\mathbf{w}(k+1) = \mathbf{w}(k) + \mu e(k)\mathbf{x}(k), \tag{18}$$

where $\mathbf{w}$ denotes the weight vector, μ the step size, and $\mathbf{x}(k)$ the input vector.

However, the traditional LMS algorithm requires the adjustment of a high-dimensional weight vector, leading to high computational complexity and making real-time control challenging in CCR-BIM applications.

In this study, dimensionality reduction is applied to retain only two key weight parameters related to the fundamental harmonic component: amplitude weight k_p and phase weight k_i. Specifically, k_p adjusts the magnitude of the compensation force, while k_i controls its phase to counteract vibration lag. The step sizes μ_p and μ_i are pre-optimized using an offline gradient descent method, avoiding online computation.

More specifically, the input signal $v(k)$ is projected onto the orthogonal components of the fundamental harmonic, given by:

$$v(k) = v_\alpha(k) + jv_\beta(k). \tag{19}$$

This allows the cost function to be simplified as:

$$\min_{k_p,k_i} E\left[\left(v_{ref}(k) - (k_p v_\alpha(k) + k_i v_\beta(k))\right)^2\right]. \tag{20}$$

Here, the estimation error is defined as the difference between the reference displacement $v_{ref}(k)$ and the estimated compensation output $k_p v_\alpha(k) + k_i v_\beta(k)$. This formulation allows the LMS algorithm to adaptively minimize the vibration deviation.

With the objective of minimizing the mean square displacement error, formulated as:

$$J(k_p, k_i) = E\left[\left(e(k) - k_p v_\alpha(k) - k_i v_\beta(k)\right)^2\right]. \tag{21}$$

The adaptive weights k_p and k_i are updated online using the gradient descent method:

$$\begin{cases} k_p(k+1) = k_p(k) + \mu_p e(k) v_h(k) \\ k_i(k+1) = k_i(k) + \mu_i e(k)\frac{dv_h(k)}{dt} \end{cases}, \tag{22}$$

where μ_p and μ_i serve as step-size factors. To ensure both rapid convergence and steady-state accuracy, μ_p and μ_i are first pre-optimized offline to obtain baseline values (μ_{p0}, μ_{i0}). During online operation, they are further adjusted adaptively according to the instantaneous error magnitude $e(k)$:

$$\begin{cases} \mu_p(k) = \frac{\mu_{p0}}{1+\beta|e(k)|} \\ \mu_i(k) = \frac{\mu_{i0}}{1+\beta|e(k)|} \end{cases}, \tag{23}$$

where β is a tuning factor. This mechanism enables fast convergence under large errors and improved steady-state precision when the error is small. To guarantee stability, the instantaneous step sizes must also satisfy the following convergence condition:

$$\begin{cases} 0 < \mu_p < \frac{2}{\lambda_{\max}(R_p)} \\ 0 < \mu_i < \frac{2}{\lambda_{\max}(R_i)} \end{cases}, \tag{24}$$

where $R_p = E[v_h(k)v_h^T(k)]$ and $R_i = E[\dot{v}_h(k)\dot{v}_h^T(k)]$ denote the autocorrelation matrices of the input signals, and $\lambda_{\max}$ represents the maximum eigenvalue. By constraining the step size with $\lambda_{\max}$, parameter divergence is avoided.

The convergence behavior of the adaptive weights $k_p(k)$ and $k_i(k)$ under VSS-ALMS algorithm is shown in Fig. 7. As can be observed, both parameters gradually approach their optimal values through iterative updates, indicating effective amplitude and phase adaptation. This online convergence ensures real-time tracking of rotor vibration characteristics despite load disturbances and speed fluctuations.

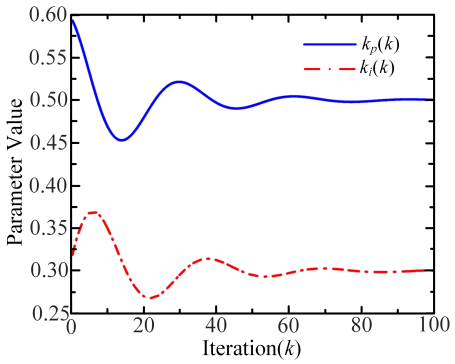

FIGURE 7. Adaptive convergence trajectories of LMS parameters $k_p(k)$ and $k_i(k)$ during online compensation force adjustment.

The synergy between RA-SOGI and VSS-ALMS algorithm enables real-time compensation without matrix operations, which is critical for high-speed CCR-BIM with limited DSP resources. This leads to the compensation force generation in Eq. (25).

3.2.2. Compensation Force Generation and Parameter Update

The compensation force signal is generated from the fundamental harmonic component $v_h(k)$ and adaptive parameters, expressed as:

$$F_{\mathbf{comp}}(k) = k_p(k)v_h(k) + k_i(k)\frac{dv_h(k)}{dt}, \tag{25}$$

where k_p acts as a proportional gain that dynamically adjusts the amplitude of the compensation force in proportion to the vibration amplitude; k_i serves as an integral gain that adjusts the phase of the compensation force to counteract the vibration lag angle γ. This compensation force directly cancels the fundamental vibration component synchronized with ω_m, with its amplitude and phase adaptively tuned through k_p and k_i, effectively suppressing lag effects caused by speed fluctuations.

3.2.3. Adaptive PID with Variable Learning Rates and Residual Feedforward

To further suppress residual errors after feedforward compensation, a feedback channel employs an enhanced adaptive PID

controller. Unlike conventional adaptive PID methods with fixed update rates, the proposed scheme introduces variable learning rates that adjust dynamically according to the instantaneous error magnitude, ensuring both rapid convergence under large disturbances and high steady-state precision. In addition, a residual feedforward correction term derived from the harmonic observer is incorporated, which allows the PID controller to anticipate unmodeled dynamics and improve compensation accuracy.

Using the sensitivity function approximation method, the update laws for K_p, K_i, and K_d are defined as:

$$\begin{cases} K_p(k+1) = K_p(k) + \alpha_p(k) e_{\mathbf{PID}}(k) v_h(k) + \kappa_p \hat{r}(k) \\ K_i(k+1) = K_i(k) + \alpha_i(k) e_{\mathbf{PID}}(k) \sum v_h(k) + \kappa_i \hat{r}(k) \\ K_d(k+1) = K_d(k) + \alpha_d(k) e_{\mathbf{PID}}(k) \frac{dv_h(k)}{dt} + \kappa_d \hat{r}(k) \end{cases}, \tag{26}$$

where $\alpha_p(k)$, $\alpha_i(k)$, and $\alpha_d(k)$ are variable learning rates defined as:

$$\alpha_j(k) = \frac{\alpha_{j0}}{1 + \gamma |e_{\mathbf{PID}}(k)|}, \quad j \in \{p, i, d\}, \tag{27}$$

with α_{j0} denoting baseline values obtained offline and γ a tuning factor. $\hat{r}(k)$ is the residual signal estimated from the harmonic observer, used to provide an anticipatory correction. κ_p, κ_i, and κ_d are small feedforward gains for residual injection.

The term $\frac{dv_h(k)}{dt}$ in Eq. (26) is approximated using a first-order backward difference method as $\frac{v_h(k) - v_h(k-1)}{T}$, where T is the sampling period. This allows for real-time implementation in a discrete-time control system.

This mechanism allows fast adaptation when the error is large while improving steady-state precision as the error decreases.

The enhanced PID control force is defined as:

$$\begin{aligned} F_{\mathbf{PID}}(k) &= K_p(k) e_{\mathbf{PID}}(k) + K_i(k) \int e_{\mathbf{PID}}(k) dt \\ &\quad + K_d(k) \frac{de_{\mathbf{PID}}(k)}{dt} + K_f \hat{r}(k). \end{aligned} \tag{28}$$

The input to the adaptive PID controller is the residual error $e_{\mathrm{PID}}(k)$ after feedforward compensation. The output control force $F_{\mathrm{PID}}(k)$ is then combined with the feedforward compensation force $F_{\mathrm{comp}}(k)$ to generate the total control force, and the total control force becomes:

$$F_{\mathbf{total}}(k) = F_{\mathbf{comp}}(k) + F_{\mathbf{PID}}(k), \tag{29}$$

Compared with conventional adaptive PID control, the proposed design improves robustness by incorporating variable learning rates to balance convergence speed and steady-state accuracy, along with residual feedforward correction for anticipatory compensation of unmodeled vibration components.

3.3. Lyapunov Stability Analysis

To analyze the stability of the proposed adaptive vibration compensation scheme, we define the following Lyapunov energy function:

$$V(k) = \frac{1}{2} \left[\tilde{k}_p^2(k) + \tilde{k}_i^2(k) + e(k)^2 \right], \tag{30}$$

where $\tilde{k}_p(k) = k_p(k) - k_p^*$, $\tilde{k}_i(k) = k_i(k) - k_i^*$, and $e(k)$ is the vibration displacement error.

Substituting the adaptive update laws of (22) into the difference $\Delta V(k) = V(k+1) - V(k)$:

$$\begin{cases} k_p(k+1) = k_p(k) + \mu_p(k) e(k) v_\alpha(k) \\ k_i(k+1) = k_i(k) + \mu_i(k) e(k) v_\beta(k) \end{cases}, \tag{31}$$

Equation (32) is obtained:

$$\begin{cases} \tilde{k}_p(k+1) = \tilde{k}_p(k) + \mu_p(k) e(k) v_\alpha(k) \\ \tilde{k}_i(k+1) = \tilde{k}_i(k) + \mu_i(k) e(k) v_\beta(k) \end{cases}, \tag{32}$$

The Lyapunov difference is then given by:

$$\begin{aligned} \Delta V(k) &= V(k+1) - V(k) \\ &= \frac{1}{2} \begin{bmatrix} \tilde{k}_p^2(k+1) - \tilde{k}_p^2(k) + \tilde{k}_i^2(k+1) \\ -\tilde{k}_i^2(k) + e^2(k+1) - e^2(k) \end{bmatrix}, \end{aligned} \tag{33}$$

Assuming that the tracking error varies slowly near steady-state, the difference term $e(k+1)^2 - e(k)^2$ can be neglected, yielding:

$$\begin{aligned} \Delta V(k) \approx\ & \mu_p(k) \tilde{k}_p(k) e(k) v_\alpha(k) \\ & + \mu_i(k) \tilde{k}_i(k) e(k) v_\beta(k) + \tfrac{1}{2} \mu_p^2(k) e^2(k) v_\alpha^2(k) \\ & + \tfrac{1}{2} \mu_i^2(k) e^2(k) v_\beta^2(k), \end{aligned} \tag{34}$$

By choosing sufficiently small variable step sizes μ_p and μ_i, the higher-order terms can be suppressed, and the negative terms dominate, leading to

$$\Delta V(k) < 0 \quad \textbf{for all} \quad k \neq k^*, \tag{35}$$

Therefore, under the condition

$$\begin{cases} 0 < \mu_p(k) < \frac{2}{\lambda_{\max}(R_p)} \\ 0 < \mu_i(k) < \frac{2}{\lambda_{\max}(R_i)} \end{cases}, \tag{36}$$

the system is globally asymptotically stable in the sense of Lyapunov. Here $R_p = E[v_h(k) v_h^T(k)]$ and $R_i = E[\dot{v}_h(k) \dot{v}_h^T(k)]$ are the autocorrelation matrices, and $\lambda_{\max}$ denotes their maximum eigenvalues. It is worth noting that the residual feedforward term introduced in Section 3.2.3 does not alter the stability proof, as it can be regarded as an auxiliary bounded input that only enhances the convergence rate.

Figure 8 illustrates the time evolution of Lyapunov energy function $V(k)$ under different step-size settings μ. As expected, a smaller step size leads to slower convergence, whereas an excessively large step size results in oscillations and possible divergence. These results confirm that, when the step sizes μ_p

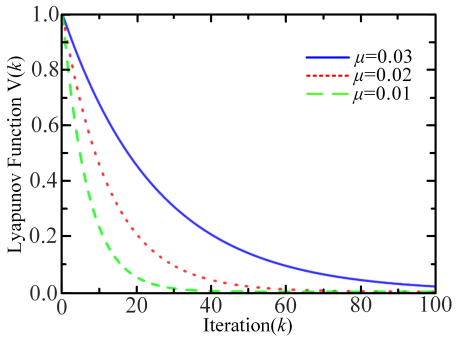

FIGURE 8. Evolution of Lyapunov function $V(k)$ under different step sizes μ.

and μ_i are properly selected within the Lyapunov stable region, the system achieves global asymptotic stability. In this simulation, μ denotes the adaptive step size (i.e., μ_p and μ_i in the controller). The chosen practical values $\mu = 0.02$ and $\mu = 0.01$ fall well inside the stability boundary, while the observation of non-convergent behavior at $\mu = 0.03$ verifies the theoretical limit predicted by Equation (36). Moreover, since the proposed scheme adopts variable step sizes, this stability guarantee extends naturally to the adaptive case.

The adaptive compensation process is collaboratively executed across three stages: (1) Initialization Stage: Set initial values for compensation parameters (k_p, k_i), adaptive PID gains (K_p, K_i, K_d), and load pre-trained step-size factors (μ_p, μ_i). (2) Real-Time Update Stage: Extract harmonic signals using the RA-SOGI observer and update parameters online through the VSS-ALMS algorithm, thereby dynamically adjusting the amplitude and phase of the feedforward compensation force Fcomp. (3) Closed-Loop Feedback Stage: Use residual errors after feedforward cancellation as input to the adaptive PID controller with residual feedforward correction, generating refined control forces FPID. The final output force is synthesized as F_{total}, ensuring effective vibration suppression. The overall flow of the self-adaptive compensation process with parameter tuning and closed-loop feedback is illustrated in Fig. 9.

The proposed hybrid vibration compensation framework, combining harmonic observation, adaptive feedforward cancellation, and closed-loop PID refinement, effectively mitigates rotor unbalance in real time with theoretical convergence guarantees, forming the control foundation of this study.

4. EXPERIMENTAL VALIDATION AND RESULTS ANALYSIS

To validate the effectiveness of the proposed compensation method, a series of comparative suspension vibration experiments were conducted on both the simulation platform and experimental platform. To further validate the superiority of the proposed approach, we benchmarked it against three strategies: PID compensation method [16], feedforward compensation approach [18], and a baseline case without compensation. A comprehensive evaluation was then conducted, assessing performance in terms of vibration suppression, dynamic response, and robustness.

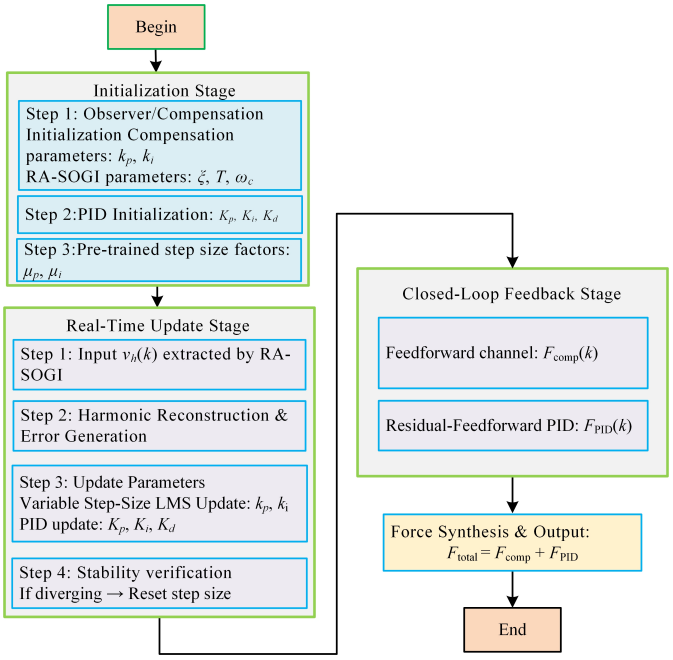

FIGURE 9. Collaborative adaptive compensation process for suspension force with parameter tuning and closed-loop feedback.

The overall block diagram of the vibration compensation control system based on the proposed strategy is shown in Fig. 10. The control system consists of two subsystems: one for the proposed suspension force vibration compensation control and the other for speed control. In the suspension force vibration compensation control scheme, the RA-SOGI module utilizes its frequency adaptive capability to achieve real-time locking of the fundamental vibration component. The feedforward channel accurately cancels out the fundamental vibration force, while the feedback channel further suppresses residual errors through a residual-feedforward adaptive PID controller. This integrated approach enables high-precision vibration compensation and stable suspension control of the CCR-BIM. Speed control adopts a conventional air-gap flux orientation control strategy [32]. The initial control parameters are provided in Table 1.

TABLE 1. Initial control algorithm parameters.

Parameters	Values	Parameters	Values
μ_p	0.02	K_p	0.5
μ_i	0.01	K_i	0.3
μ_{p0}	0.02	K_d	0.1
μ_{i0}	0.01	β	0.1
ξ_0	0.8	δ	0.4

Note: μ_p and μ_i: step-size factors for amplitude and phase adaptation; μ_{p0} and μ_{i0}: baseline step sizes; β: tuning factor for adaptive convergence; ξ_0: baseline damping ratio; δ: maximum damping variation; K_p, K_i, and K_d: proportional, integral, and derivative gains of the adaptive PID controller.

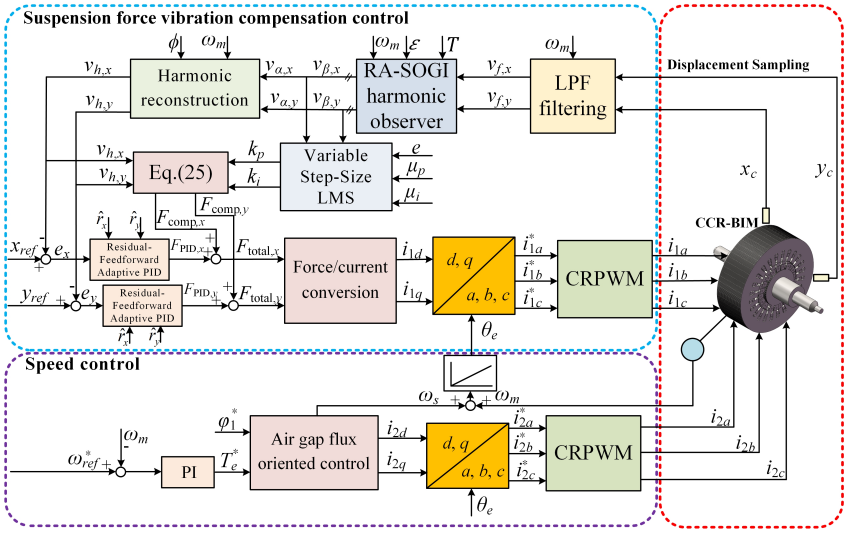

FIGURE 10. Proposed control block diagram of RA-SOGI-based dual-channel PID

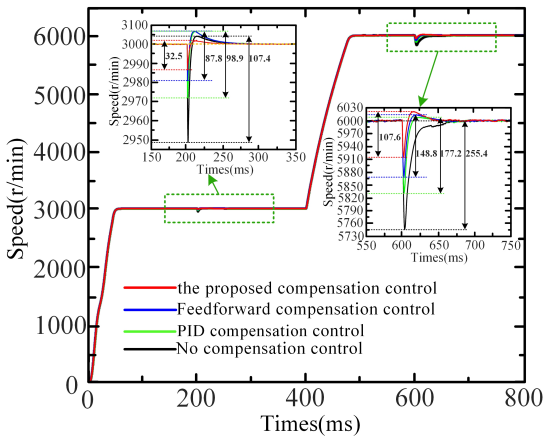

FIGURE 11. Simulated speed waveforms under sudden load disturbances.

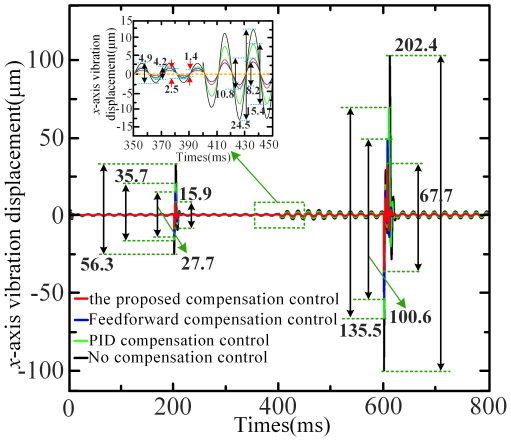

FIGURE 12. Simulated x-axis vibration displacement waveforms under four control strategies.

4.1. Simulation Verification

Figure 11 presents the simulated comparison waveforms of the speed under four compensation control strategies: no compensation control, PID compensation control, feedforward compensation control, and the proposed compensation control. The performance of these strategies was evaluated at two speeds, 3000 r/min and 6000 r/min, to analyze the effect of rotor vibration compensation under different speed conditions.

The motor started from 0 r/min and stabilized at 3000 r/min, and then a 10 Nm load was suddenly added at 200 ms. The results show that without compensation control, the speed change was 107.4 r/min; with PID compensation control, it was 98.9 r/min; with feedforward compensation control, it was 87.8 r/min; and with the proposed compensation control, it was only 32.5 r/min. Compared with no compensation control, PID compensation control, and feedforward compensation control, the proposed method reduced vibration by 69.7%, 67.1%, and 63.0%, respectively. When operating at 6000 r/min, a 10 Nm load was suddenly added at 600 ms. Without compensation control, the speed change was 255.4 r/min; with PID compensation control, it was 177.2 r/min; with feedforward compensation control, it was 148.8 r/min; and with the proposed compensation control, it was 107.6 r/min. Compared with no compensation control, PID compensation control, and feedforward compensation control, the proposed method reduced vibration by 57.9%, 39.3%, and 27.7%, respectively.

Figure 12 presents the simulated comparison waveforms of the x-axis vibration amplitudes under four compensation control strategies: no compensation control, PID compensation control, feedforward compensation control, and the proposed compensation control. At 3000 r/min, the x-axis displacement vibration amplitudes for the four control methods are 4.9 μm, 4.2 μm, 2.5 μm, and 1.4 μm, respectively. Compared to no compensation control, PID compensation control, and feedforward compensation control, the proposed compensation control reduces the x-axis vibration amplitude by 71.4%, 66.7%, and 44.0%, respectively. When a sudden load of 10 Nm is applied at 200 ms, the x-axis displacement deviation amplitudes

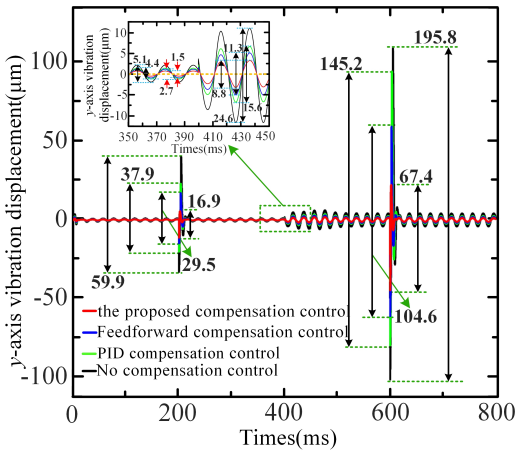

FIGURE 13. Simulated y-axis vibration displacement waveforms under four control strategies

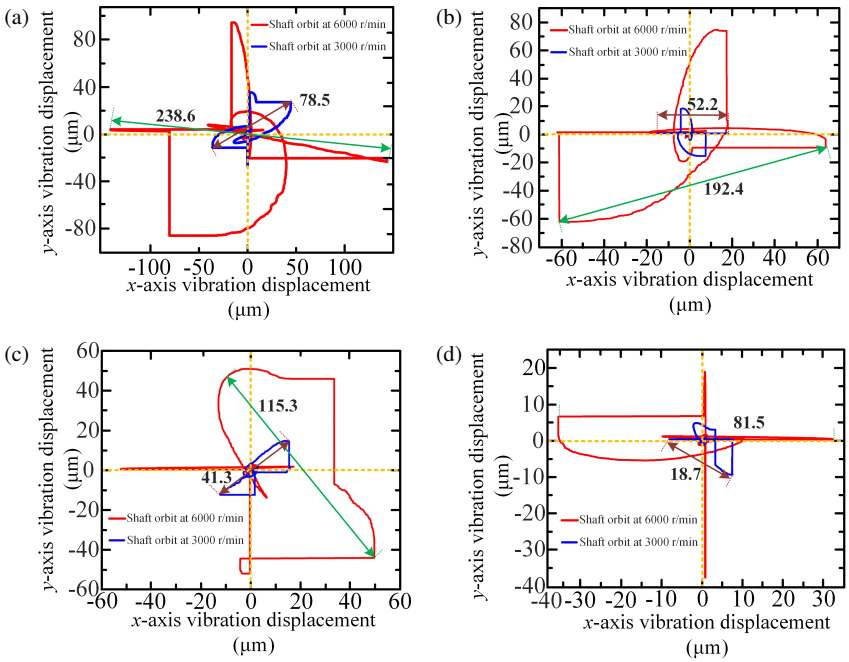

FIGURE 14. Simulated rotor trajectory waveforms under four control strategies.

for the four control methods are 56.3 μm, 35.7 μm, 27.7 μm, and 15.9 μm, respectively. The proposed compensation control reduces the deviation amplitude by 71.8%, 55.5%, and 42.6% compared to the other three methods. At 6000 r/min, the x-axis vibration amplitudes for the four control methods are 24.5 μm, 15.4 μm, 10.8 μm, and 8.2 μm, respectively. The proposed compensation control achieves reductions of 66.5%, 46.8%, and 24.1% compared to the other methods. When a sudden load of 10 Nm is applied at 600 ms, the x-axis displacement deviation amplitudes are 202.4 μm, 135.5 μm, 100.6 μm, and 67.7 μm, respectively. The proposed compensation control reduces the x-axis vibration amplitude by 66.6%, 50.0%, and 32.7% compared to the other three methods.

Figure 13 presents the simulated comparison waveforms of the y-axis vibration amplitudes under four compensation control strategies: no compensation control, PID compensation control, feedforward compensation control, and the proposed compensation control. At 3000 r/min, the y-axis displacement vibration amplitudes for the four control methods are 5.1 μm, 4.4 μm, 2.7 μm, and 1.5 μm, respectively. Compared to no compensation control, PID compensation control, and feedforward compensation control, the proposed compensation control reduces the y-axis vibration amplitude by 70.6%, 65.9%, and 44.4%, respectively. When a sudden load of 10 Nm is applied at 200 ms, the y-axis displacement deviation amplitudes for the four control methods are 59.9 μm, 37.9 μm, 29.5 μm, and 16.9 μm, respectively. The proposed compensation control reduces the deviation amplitude by 71.8%, 55.4%, and 42.7% compared to the other three methods. At 6000 r/min, the y-axis vibration amplitudes for the four control methods are 24.6 μm, 15.6 μm, 11.3 μm, and 8.8 μm, respectively. The proposed compensation control achieves reductions of 64.2%,

TABLE 2. Electrical and mechanical parameters of the proposed CCR-BIM.

Parameter items	Value	
Rotor mass m/kg	2.97	
Outer diameter of the stator/mm	128	
Stator inner diameter/mm	65	
Stack length/mm	83	
Moment of inertia J/g · m^2	7.74	
Rotor eccentricity Δr/μm	0.5	
Sampling period T/s	0.0001	
Parameter items	**Parameters of torque winding**	**Parameters of suspension force winding**
Pole pairs p	1	2
Rated power (P_1/P_2)	2 kW	0.5 kW
Rated frequency/Hz	50	50
Rotor resistance/Ω	11.64	0.082
Stator resistance/Ω	2.12	1.11
Mutual inductance/mH	158.73	9.51
Rotor leakage inductance/mH	9.34	5.53
Turn number (Z_1/Z_2)	60	30

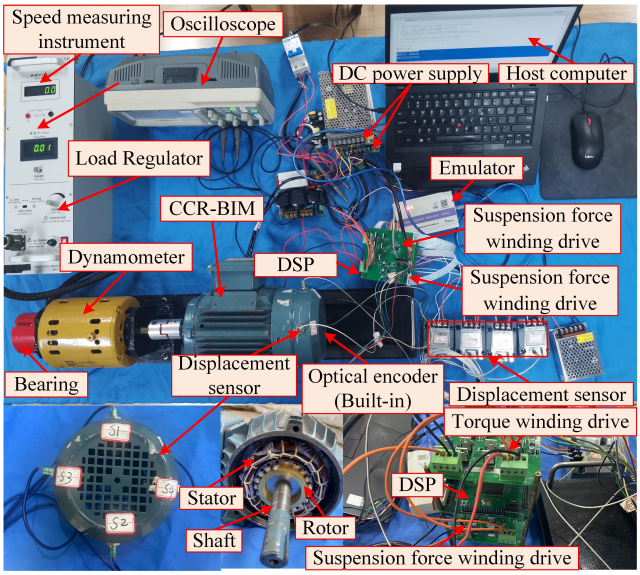

FIGURE 15. Experimental test bench for CCR-BIM.

43.6%, and 22.1% compared to the other methods. When a sudden load of 10 Nm is applied at 600 ms, the y-axis displacement deviation amplitudes are 195.8 μm, 145.2 μm, 104.6 μm, and 67.4 μm, respectively. The proposed compensation control reduces the y-axis vibration amplitude by 65.6%, 53.6%, and 35.6% compared to the other three methods.

Figure 14 presents simulated rotor shaft-end trajectory curves under four compensation control methods, demonstrating significant performance improvements at both 3000 r/min and 6000 r/min operating speeds. The maximum trajectory values were measured at 81.6 μm and 238.6 μm with no compensation control, which reduced to 52.2 μm and 192.4 μm with PID compensation control, and further decreased to 41.3 μm and 115.3 μm using feedforward compensation. Most notably, the proposed compensation control achieved superior results of just 18.7 μm and 81.5 μm maximum trajectory values at these respective speeds. Quantitative analysis reveals the proposed method reduced maximum shaft-end trajectory by 77.1%, 64.2%, and 54.7% compared to no compensation, PID compensation, and feedforward compensation at 3000 r/min, with corresponding reductions of 65.8%, 57.6%, and 29.3% observed at 6000 r/min. These substantial reductions in trajectory amplitude confirm the method's effectiveness in optimizing rotor motion under high-speed conditions while significantly mitigating mechanical wear risks.

4.2. Experimental Verification

To validate the effectiveness of the proposed algorithm, an experimental platform was built as shown in Fig. 15. Its core components include a TMS320F28335 DSP controller, a CCR-BIM prototype, an optical encoder, eddy current sensors, a three-phase full-bridge inverter drive module, and driver boards for both the suspension force winding and torque winding. These components together serve to verify the performance of the proposed vibration compensation control strategy. The parameters of the CCR-BIM prototype in the experimental platform are shown in Table 2.

Figure 16 illustrates the comparison of speed dynamic response characteristics among four compensation control strategies: no compensation control, PID compensation control, feedforward compensation control, and the proposed compensation control. The motor undergoes a startup process from standstill to 3000 r/min, followed by further acceleration to 6000 r/min. The performance of rotor vibration suppression is

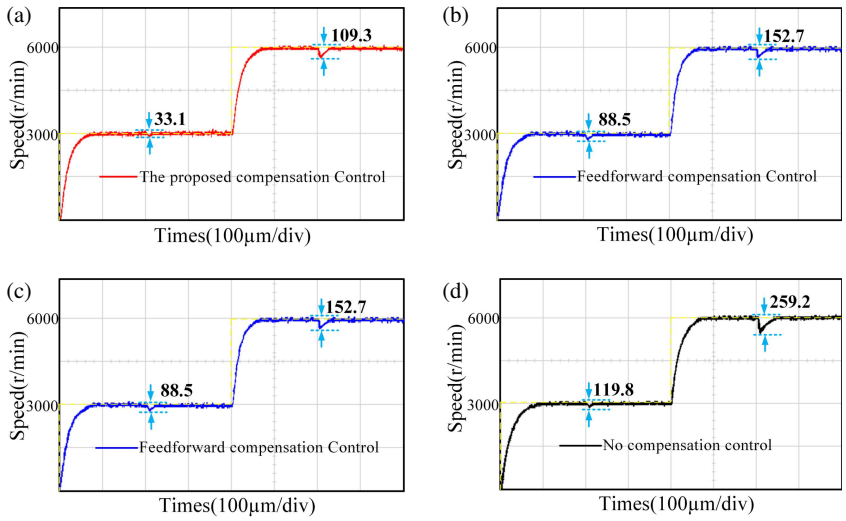

FIGURE 16. Experimental speed waveforms under sudden load disturbances. (a) The proposed compensation control, (b) Feedforward compensation control, (c) PID compensation control, (d) No compensation control.

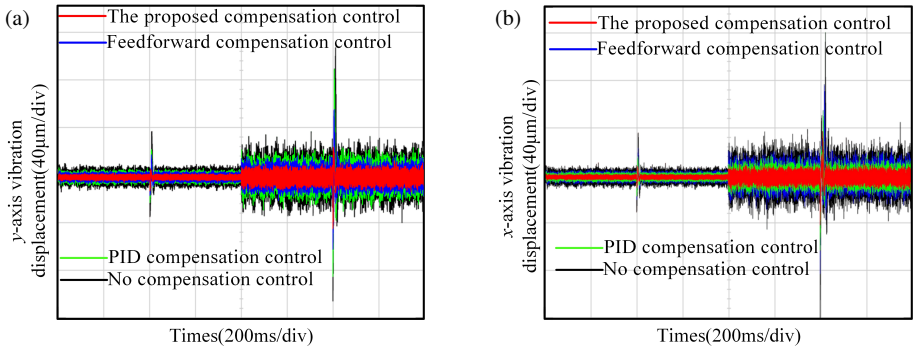

FIGURE 17. Experimental waveforms of x-axis and y-axis vibration displacement under four control strategies. (a) x-axis, (b) y-axis.

evaluated and compared across these speed ranges. Under a step load disturbance of 10 Nm applied during operation, the proposed compensation control demonstrates a significant reduction in speed variation compared to all benchmark methods. This improvement is consistently observed at both 3000 r/min and 6000 r/min, confirming the robustness and superior dynamic performance of the proposed approach across different operating speeds.

Figures 17(a) and 17(b) present a comprehensive experimental comparison of vibration displacement along both the x- and y-axis under sudden loading and variable speed conditions for four control strategies: no compensation control, PID compensation control, feedforward compensation control, and the proposed compensation control. The proposed control strategy demonstrates consistent superiority in vibration suppression performance across all tested conditions. It significantly reduces both vibration amplitude and peak-to-peak deviation compared to benchmark methods during sudden load disturbances and speed variations. The method exhibits the most stable dynamic response and lowest vibration levels, confirming its effectiveness in enhancing operational precision and disturbance rejection capability throughout the entire operating range.

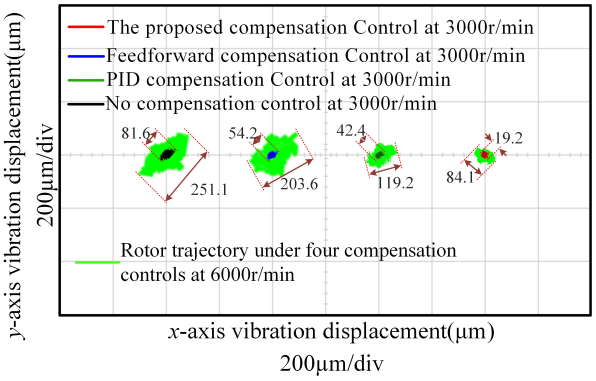

FIGURE 18. Experimental rotor trajectory waveforms under four control strategies.

Figure 18 compares the experimental rotor shaft end trajectories under four compensation control methods at both 3000 r/min and 6000 r/min speed. The proposed compensation control consistently achieves the most confined and stable trajectory among all methods at both speed conditions. It demonstrates a substantial reduction in trajectory amplitude compared to uncompensated, PID-compensated, and feedforward-

compensated systems, with particularly notable improvement at higher rotational speed. These results confirm the method's effectiveness in optimizing rotor motion precision and reducing mechanical wear risk across medium and high-speed operating conditions.

The experimental results demonstrate that the proposed composite control method, which integrates an SOGI harmonic observer with adaptive PID, effectively attenuates speed fluctuations induced by sudden load disturbances. The method achieves significant suppression of vibration amplitudes along both the x- and y-axis compared to conventional feedforward compensation and uncompensated control, indicating robust multi-directional vibration rejection and improved system stability. Furthermore, a notable reduction in peak trajectory deviation is consistently observed across operating conditions.

In summary, the proposed approach exhibits superior performance in vibration suppression, dynamic response, and trajectory stability, particularly under high-speed operation and transient load scenarios. These results conclusively validate the effectiveness of the proposed hybrid control strategy in enhancing the dynamic performance, vibrational integrity, and operational stability of CCR-BIM systems. The method demonstrates strong potential for applications requiring high precision and robustness under demanding operational conditions.

5. CONCLUSIONS

In this paper, an enhanced vibration compensation strategy for composite cage rotor bearingless induction motors (CCR-BIM) was proposed. The method integrates an RA-SOGI with VSS-ALMS optimization for real-time harmonic extraction and a residual-feedforward adaptive PID controller with variable learning rates for dual-channel compensation. This hybrid design not only preserves the observation capability of the RA-SOGI but also reduces computational complexity through quadrature-demodulation-based realization, while the adaptive PID achieves superior balance between dynamic responsiveness and steady-state accuracy. The major findings are summarized as follows:

(1) RA-SOGI with nonlinear damping and frequency tracking enables fast and accurate locking of the fundamental vibration component without complex parameter tuning, significantly improving robustness against rotor speed fluctuations and external disturbances.

(2) VSS-ALMS optimization dynamically adjusts the amplitude and phase of the compensation force with reduced computational burden, ensuring real-time convergence even under high-speed operation.

(3) Residual-feedforward adaptive PID feedback achieves a superior balance between transient response and steady-state accuracy, while the Lyapunov-based stability analysis provides rigorous proof of global asymptotic stability under practical step-size conditions.

Experimental results demonstrate its superior performance in suppressing vibrations under dynamic disturbances.

Future work will extend this framework toward multi-harmonic vibration suppression, explore robustness under parameter uncertainties and external disturbances, and investigate hardware-oriented optimization for real-time DSP/FPGA implementation to facilitate broader industrial applications.

ACKNOWLEDGEMENT

This work was supported by Anhui Province Excellent Young Teacher Development Program (Grant No. YQYB2025025), West Anhui University Startup Fund for Outstanding Talents (Grant No. WGKQ2025006), the University-Enterprise Practical Cooperation Base of Anhui Provincial Department of Education, China (Grant No. 2024xqhz065), and the China Postdoctoral Science Foundation (Grant No. 2025M770477).

CONFLICT OF INTEREST

The authors declare that they have no competing interests.

REFERENCES

[1] Chen, J., Y. Fujii, M. W. Johnson, A. Farhan, and E. L. Severson, "Optimal design of the bearingless induction motor," *IEEE Transactions on Industry Applications*, Vol. 57, No. 2, 1375–1388, 2021.

[2] Chiba, A., D. T. Power, and M. A. Rahman, "Characteristics of a bearingless induction motor," *IEEE Transactions on Magnetics*, Vol. 27, No. 6, 5199–5201, 1991.

[3] Sun, C., Z. Yang, X. Sun, and Q. Ding, "An improved mathematical model for speed sensorless control of fixed pole bearingless induction motor," *IEEE Transactions on Industrial Electronics*, Vol. 71, No. 2, 1286–1295, 2024.

[4] Azadrou, H., "Design and optimization of a very high speed three phase bearingless induction motor," *International Journal of Industrial Electronics Control and Optimization*, Vol. 6, No. 4, 283–289, 2023.

[5] Bu, W., X. Zhang, and F. He, "Sliding mode variable structure control strategy of bearingless induction motor based on inverse system decoupling," *IEEJ Transactions on Electrical and Electronic Engineering*, Vol. 13, No. 7, 1052–1059, 2018.

[6] Su, Y., Z. Yang, X. Sun, and W. Pan, "Speed sensorless control of a bearingless induction motor based on sliding mode observer with improved double power reaching law," *International Journal of Electronics*, 1–17, 2025.

[7] Lu, C., Z. Yang, X. Sun, and Q. Ding, "Design and multi-objective optimization of a composite cage rotor bearingless induction motor," *Electronics*, Vol. 12, No. 3, 775, 2023.

[8] Du, C., C. Lu, J. Fang, J. Zhang, and J. Cheng, "A combined LPTN-FETM approach for dual-mode thermal analysis of composite cage rotor bearingless induction motor (CCR-BIM) with experimental verification," *Energies*, Vol. 18, No. 7, 1816, 2025.

[9] Lu, C., J. Cheng, Q. Ding, G. Zhang, J. Fang, L. Zhang, C. Du, and Y. Zhang, "Inverse system decoupling control of composite cage rotor bearingless induction motor based on support vector machine optimized by improved simulated annealing-genetic algorithm," *Actuators*, Vol. 14, No. 3, 125, 2025.

[10] Ye, X., X. Tang, K. Xing, H. Wang, J. Yao, and T. Zhang, "Repetitive control for vibration suppression of bearingless induction motor," *IEEE Access*, Vol. 12, 60 532–60 540, 2024.

[11] Bu, W., X. Tu, C. Lu, and Y. Pu, "Adaptive feedforward vibration compensation control strategy of bearingless induction

motor," *International Journal of Applied Electromagnetics and Mechanics*, Vol. 63, No. 2, 199–215, 2020.

[12] Yang, Z., P. Jia, X. Sun, and H. Mei, "Rotor vibration unbalance compensation control of a bearingless induction motor," *International Transactions on Electrical Energy Systems*, Vol. 31, No. 8, e12953, 2021.

[13] Wang, X. and H. Zhu, "Vibration compensation control of BPMSM with dead-time effect based on adaptive neural network band-pass filter," *IEEE Transactions on Power Electronics*, Vol. 37, No. 6, 7145–7155, 2022.

[14] Zheng, Y., N. Mo, Y. Zhou, and Z. Shi, "Unbalance compensation and automatic balance of active magnetic bearing rotor system by using iterative learning control," *IEEE Access*, Vol. 7, 122 613–122 625, 2019.

[15] Rahmatullah, R., A. Ak, and N. F. O. Serteller, "Design of sliding mode control using SVPWM modulation method for speed control of induction motor," *Transportation Research Procedia*, Vol. 70, 226–233, 2023.

[16] Lu, C., Z. Yang, X. Sun, and Q. Ding, "Vibration compensation control strategy of composite cage rotor bearingless induction motor based on fuzzy coefficient adaptive-linear-neuron method," *ISA Transactions*, Vol. 154, 455–464, 2024.

[17] Tan, C., H. Wang, and Y. Wang, "Rotor eccentricity compensation of bearingless switched reluctance motors based on extended kalman filter," in *2019 12th International Symposium on Computational Intelligence and Design (ISCID)*, Vol. 2, 111–115, Hangzhou, China, 2019.

[18] Zhu, H., Z. Yang, X. Sun, D. Wang, and X. Chen, "Rotor vibration control of a bearingless induction motor based on unbalanced force feed-forward compensation and current compensation," *IEEE Access*, Vol. 8, 12 988–12 998, 2020.

[19] Mao, B. and H. Zhu, "Unbalance vibration suppression control of PMa-BSynRM based on total least square adaptive filtering algorithm," *IEEE Journal of Emerging and Selected Topics in Power Electronics*, Vol. 11, No. 6, 5798–5808, 2023.

[20] Bu, W., Y. Huang, C. Lu, H. Zhang, and H. Shi, "Unbalanced displacement LMS extraction algorithm and vibration control of a bearingless induction motor," *International Journal of Applied Electromagnetics and Mechanics*, Vol. 56, No. 1, 35–47, 2018.

[21] Chen, Y. and Y. Zhou, "Active disturbance rejection and ripple suppression control strategy with model compensation of single-winding bearingless flux-switching permanent magnet motor," *IEEE Transactions on Industrial Electronics*, Vol. 69, No. 8, 7708–7719, 2022.

[22] Shen, L., D. Jiang, and H. Zhu, "Control study for suppressing rotor vibration of the six-pole hybrid magnetic bearing system based on no-parameter variable-step-size least-mean-square algorithm," *IEEE Transactions on Power Electronics*, Vol. 40, No. 8, 10 672–10 681, 2025.

[23] Lu, C., Q. Ding, Z. Liu, G. Zhang, J. Fang, J. Cheng, and Y. Zhang, "A collaborative fault-tolerant strategy for displacement sensors in CCR-BIM: Dynamic kernel width optimization of AGRNN and ring-shaped redundancy," *IEEE Journal of Emerging and Selected Topics in Power Electronics*, 1–1, 2025.

[24] Mao, B., D. Jiang, H. Zhu, and J. Ju, "Speed sensorless control of permanent magnet-assisted bearingless synchronous reluctance motor based on enhanced linear extended state observer," *Electrical Engineering*, Vol. 107, No. 4, 4381–4392, 2025.

[25] Liu, Z., X. Wu, J. Cai, Y. Yang, and C. Liu, "Decoupled topologies and radial levitation control of a novel permanent magnet biased bearingless switched reluctance motor," *IEEE Transactions on Industrial Electronics*, Vol. 72, No. 4, 3370–3380, 2025.

[26] Pei, T., D. Li, J. Liu, J. Li, and W. Kong, "Review of bearingless synchronous motors: Principle and topology," *IEEE Transactions on Transportation Electrification*, Vol. 8, No. 3, 3489–3502, 2022.

[27] Yang, Z., C. Lu, X. Sun, J. Ji, and Q. Ding, "Study on active disturbance rejection control of a bearingless induction motor based on an improved particle swarm optimization-genetic algorithm," *IEEE Transactions on Transportation Electrification*, Vol. 7, No. 2, 694–705, 2021.

[28] Zhao, R., Z. Xin, P. C. Loh, and F. Blaabjerg, "A novel flux estimator based on multiple second-order generalized integrators and frequency-locked loop for induction motor drives," *IEEE Transactions on Power Electronics*, Vol. 32, No. 8, 6286–6296, 2017.

[29] Wang, G., L. Ding, Z. Li, J. Xu, G. Zhang, H. Zhan, R. Ni, and D. Xu, "Enhanced position observer using second-order generalized integrator for sensorless interior permanent magnet synchronous motor drives," *IEEE Transactions on Energy Conversion*, Vol. 29, No. 2, 486–495, 2014.

[30] Karchi, N., D. Kulkarni, R. P. d. Prado, P. B. Divakarachari, S. N. Patil, and V. Desai, "Adaptive least mean square controller for power quality enhancement in solar photovoltaic system," *Energies*, Vol. 15, No. 23, 8909, 2022.

[31] Tang, Z. and B. Akin, "A new LMS algorithm based deadtime compensation method for PMSM FOC drives," *IEEE Transactions on Industry Applications*, Vol. 54, No. 6, 6472–6484, 2018.

[32] Bu, W., X. Cheng, F. He, Y. Qiao, H. Zhang, and X. Xu, "Inverse system modeling and decoupling control of bearingless induction motor based on air gap flux orientation," *International Journal of Applied Electromagnetics and Mechanics*, Vol. 53, No. 3, 567–577, Mar. 2017.